PCCP

Accepted Manuscript

ROYAL SOCIETY OF CHEMISTRY

www.rsc.org/pccp

Physical Chemistry Chemical Physics
CREATED USING THE RSC LaTeX PCCP ARTICLE TEMPLATE – SEE www.rsc.org/electronicfiles FOR DETAILS
ARTICLE TYPE www. rsc.org/xxxxxx | XXXXXXXX

Ab-initio Calculation of Electronic Charge Mobility in Metal-Organic Frameworks

Terence Musho,*[a] and Nianqiang Wu[a]

Received Xth XXXXXXXXXX 20XX, Accepted Xth XXXXXXXXX 20XX
First published on the web Xth XXXXXXXXXX 200X
DOI: 10.1039/b000000x

A density functional theory approach coupled with Boltzmann transport equation within the relaxation time approximation was used to investigate the charge mobility for three MOF functionalization designs. The specific MOF investigated was a Zr-UiO-66 MOF with three functionalizations that included a benzenedicarboxylate (BDC), BDC functionalized with an amino group (BDC+NH_2), and BDC functionalized with nitro group (BDC+NO_2). Previous experimental studies have confirmed a 40% decrease in the optical band-gap with functionization; this study predicted an accompanying decrease in mobility by 14%. Contrary, the charge density was found to increase with functionalization. The culmination of these two findings resulted in a predicted conductivity of approximately 3.8x10^{-8} S/cm for BDC design and decreasing less than 2% for other cases. Furthermore, band conduction was confirmed for this MOF design as a result of the de-localized π electron of the carbon atoms along the organic linker. Overall, the functionalization proved to decrease mobility; however, it was evident that the functionalization has potential for tailoring the spectral layout of low lying unoccupied orbitals and ultimately the charge concentration, which could prove important for increasing the overall conductivity of MOFs.

1 Introduction

Metal organic frameworks have come to the forefront of the photocatalysis research because of several redeeming attributes. The most redeeming of those attributes are 1) the high area density of reaction sites compared to planar catalysis, 2) the ability to tailor the optical adsorption properties, and 3) the high selectivity of the reaction sites. At the root of these qualities is an endless design space to choose from, which makes material selection a daunting, but necessary task to optimize a photocatalysis device construction. An additional attribute that is often overlooked when designing a high performing photocatalyst material is related to the charge carrier mobility. Recent studies indicated that conductivity of MOFs can be changed over six orders of magnitudes depending on the funcationalization and associated metalloid[1–3]. Other studies have demonstrated the conductivity can be furthermore be controlled by increasing the infiltration of the MOF[4]. Both approaches provide a material system with endless tailorability with applications in new electric and opto-electronic devices[5]. In this study, it is hypothesized that conductivity can be controlled through sole functionalization of the MOF linkers. This assumes that the majority carrier will exhibit band conduction that can be tailored through functionalization. Therefore, this research is aimed at investigating the electron mobility in a long-ranged ordered metal-organic framework material under three different functionalizations.

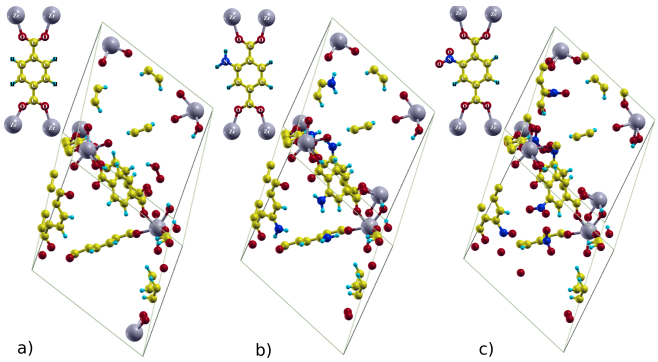

Fig. 1 Illustration of the three primitive unit cells of the studied metal organic framework material. Each MOF framework is based on Zr-UiO-66 design[6] and the linker design is a) benzenedicarboxylate (BDC), b) BDC functionalized with NH2 (BDC+NH2), and c) BDC functionalized with NO2 (BDC+NO2).

The ability to tailor the optical absorption properties of the MOF based material have been demonstrated from both a experimental point-of-view[7,8] and a theoretical point of view[9]. These findings confirm that the functionalization does decrease the optical band gap. There is evidence to suggest that the same functionalization should also influence the mobility of the charge carriers[10,11]. Compound this with the long-range order of MOF structures, there is a possibility for high mobil-

[a] *Department of Mechanical and Aerospace Engineering, West Virginia University, Morgantown, WV 26506-6106, USA. Fax: 304-293-6689; Tel: 304-293-3256; E-mail: tdmusho@mail.wvu.edu*

ity charge pathways that can be tailored[1]. In selecting a base framework it was found that there is a limited number of MOF structures with intrinsic mobility. For the cases where there is intrinsic mobility, the carrier mechanism in these MOF materials is based on two dominate transport modes. The first mode is the mobility of delocalized electrons, which exhibit band conduction or electron tunneling. This is synonymous to the transport found in small length molecular junction. The second mode is a charge hopping mechanism, which is typical for truly organic materials that have localized charges[12]. There is often a trade-off between these two mechanisms. At shorter molecular lengths, the transport is dominated by tunneling and at larger molecular lengths, the transport is governed by electron hopping. The first mechanism is the most interesting as this research looks to take advantage of the delocalized π electron in the aromatic carbon ring by modifying their electronic environment through functionalization. It is noted by others[13] that the charge mobility as result of band type motion can be difficult because the charges are localized and the curvature of the bands are often flat. These flat bands are associated with high effective masses and resemble defect or localized states providing justification for using hopping theory. However, it is hypothesized that the curvature of these bands or the effective mass, which is related to the lowest lying unoccupied states can be tailored through functionalization of the organic linkers.

In this study the objective is the understand the influence of the MOF functionalization on the charge mobility. The specific MOF and linker designs of a Zr-UiO-66 MOF[14] that include a benzenedicarboxylate (BDC), BDC functionalized with an amino group[15] (BDC+NH_2), and BDC functionalized with nitro group (BDC+NO_2). The primitive unit cell of the three linker designs are illustrated in Figure 1. The primitive unit cell contains approximately 114 atoms. The nominal lattice constant (a) for all of the MOF designs is 14.74Å. The space group is cubic $\bar{4}3m$. See the supplemental CIF file for more detailed description of the unit cell. Similar CIF descriptions can also be found in the literature[16].

2 Computational Details

The computational calculations were carried out using Quantum Espresso plane-wave Density Functional Theory. A psuedopotential approach was used to alleviate the computational expense. The functional form of the pseudo-wave functions were based on Perdew-Burke-Ernzerhof (PBE) ultrasoft potentials. The reader should note of the known issue for DFT to under predict the highest unoccupied orbitals and consequently the band gaps. Studied by others[17] have provided quantitative comparison of different functionals and have provided evidence that hybrid based functionals that include a fraction of exact exchange provide better estimates for band gap values. Previous studied of the same MOF material that investigated the band gap modulation came to the conclusion by comparison to experimental results that the PBE functional provided a better estimate compared to a BLYP functional[18]. Furthermore, these previous studied did test a hybrid functional PBE0, however, it was reasoned that the empiricism of mixing the exact exchange provides more uncertainty in the results.

The k-point mesh was sampled using a Monkhorst-Pack 4x4x4 grid with a offset 1/4,1/4,1/4 for the self-consistent calculations. The k-point mesh was sampled in a similar manner for the non-self-consistent calculation, with the exception of the shift to capture the Γ point. To account for the Van der Waals interaction, a Van der Waals correction term[19,20] was incorporated, which introduced some empiricism into the calculation. A DFT-D semi-empirical method[19,20] was used with the Quantum Espresso framework where the scaling parameter (S6) was specified to be 0.75 and cut-off radius for the dispersion interaction was 105.8 angstroms. Both the ion and unit cell geometries were relaxed to a relative total energy less than $1x10^{-10}$ and overall cell pressure of less than 0.5 kBar. Once relaxed, the induced straining of the unit cell was applied by dilatation of both the ion position and lattice parameter along the $<111>$ crystallographic direction.

3 Results and Discussion

The approach taken in this study is to assume that the dominate mode of transport in these MOFs is delocalized π electrons that exhibit band conduction. In making this assumption and assuming particle based motion of the majority carriers the Boltzmann equation with a relaxation time approximation (RTA) was employed. The derivation of this equation within the relaxation time approximation was done by Bardeen and Shockley for non-polar semiconductors[21]. By rearranging the Boltzmann expression within the relaxation time approximation, the mobility expression can be written as follows,

$$\mu = \frac{q\tau_s}{m^*} = \left(\frac{C_1\hbar^4 q}{E_1 q}\right)^2 (m_e m^*)^{5/2} (Tk_B)^{3/2}, \qquad (1)$$

here C_1 is the elastic constant, E_1 is the three-dimension (3D) deformation potential, m^* is the parabolic effective mass or reduced mass, m_e is the mass of an electron, T is the temperature, and k_B is the Boltzmann constant. The mobility readily thought of as scattering rate divided by the carrier's effective mass. The right portion of Equation 1 can be thought of a closed form expression for estimating the electron-phonon scattering rate (τ_s), which is often the limiting scattering mechanism in single crystal materials. The assumption of phonon limiting scattering mechanism is phonon based dielectric studies of similar MOF materials[22,23]. The complex dielectric

Design	C_1 (N/m^2)	E_1 (eV)	Charge Concentration (cm^{-3})	Mobility (cm^2/V-s)	Conductivity (S/cm)
MOF BDC	3.0790x10^9	18.655	1.7418x10^{14}	1.3691x10^{-3}	3.8202x10^{-8}
MOF BDC+NH_2	3.3300x10^9	20.075	1.8568x10^{14}	1.2786x10^{-3}	3.8033x10^{-8}
MOF BDC+NO_2	3.5234x10^9	21.345	1.9635x10^{14}	1.1967x10^{-3}	3.7642x10^{-8}

Table 1 Predicted elastic constant (C_1), deformation potentials (E_1), and mobilities for three MOF designs at 300K. The MOF BDC+NH_2 proves to have lowest mobility, which is attributed to the largest deformation potential. MOF BDC has the largest mobility but not significantly larger than other designs.

constant provides a macroscopic view point of the dissipation. A near unity static or real portion of the dielectric constant[23] suggests that the charge carriers are highly directional and the Coulomb interaction are minimal. Additionally, nuclear magnetic resonance (NMR) studies[22] that provide an estimate of the complex portion of the dielectric indicates that there is a noticeable temperature dependence, which is governed by the phonon content. The important parameters in Equation 1 are

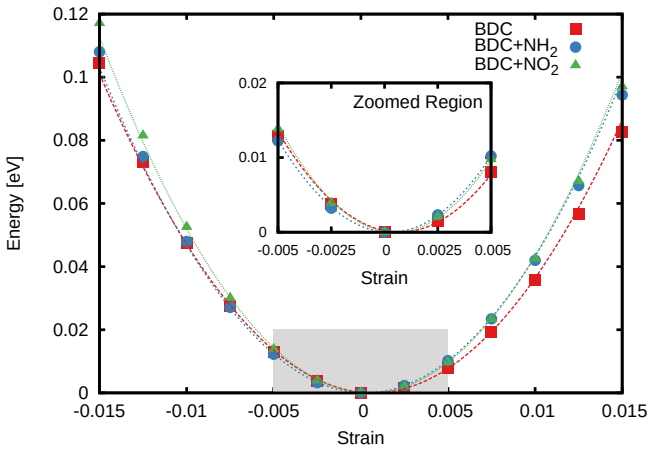

Fig. 2 Plot of the total energy as a function of <111> strain. The elastic constant was fit to the data contained within the grayed region. The dashed lines represent the parabolic elastic constant relationship. Tabulated energy values can be found in the supplemental material and the corresponding elastic constant values can be found in Table 1.

the elastic constant and acoustic deformation potential. The deformation potential relates a mechanical strain, in this case a phonon or lattice strain to a electric scattering potential. More specifically, a 3D deformation potential description is used to account for the probability of interband scattering of electron which involve a phonon to conserve momentum and energy. There is a trade off between the mobility of the majority carrier and the phonon or heat production. The other critical parameter is the elastic constant of the material, which quantifies the resistance to material deformation. Both of these parameters are empirical in nature and are often used as fitting parameters within the Boltzmann based mobility calculation. The approach taken in the research is to use DFT results to determine both of these empirical parameters.

3.1 Elastic Constant Calculation

The elastic constant of the material, C_1, can be related to the bulk modulus of the material. The bulk modulus of the material will govern sound speed of the material and ultimately the acoustic phonon content. These acoustic phonons are required for interband transitions. To determine the elastic constant of the material, a series of DFT calculations were conducted that strained the unit cell along the <111> direction. Because the charge carriers of the material is not confined within a particular direction and the strain is oriented in all three crystallographic directions, the deformation potential will be 3D deformation potential.

To determine the elastic constant, a series of thirteen cases were set-up that range from -1.5% strain (compression) to +1.5% strain (tension). Strain is determined by the following, $\varepsilon = \Delta l/l_o$, where l is stained length and l_o is the original length. The strain was applied in all three crystallographic directions and the ion positions were also displaced along these directions. The original length (l_o) is determined by the relaxed coordinate and ion positions. A self-consistent field (SCF) calculation was carried out for all thirteen strain positions and the total energy was tabulated. The results are tabulated in Table 1.

Provided the total energy at the three MOF design (see Table 1) the elastic constant was able to be calculated by relating the total energy to the strain energy. The relationship used to related the volumetric strain energy takes the following form,

$$E = \frac{1}{2}\bar{V}C_1(1+\varepsilon)\varepsilon^2 + E_0, \qquad (2)$$

where E is the total energy, $\bar{V}$ is the volume, C_1 is the elastic constant, and ε is the strain. Figure 2 is a plot of the total energy and a least square fit of Equation 2 where C_1 is the independent parameter. The elastic constant for all three design is provided in Table 1. The grayed region associated with the inset figure emphases the similarity between the three elas-

tic constants for all three designs. The average elastic constant for all three of the cases is approximately $3.3x10^9$ N/m^2. The grayed region contains the data used to fit Equation 2 because the total energy curve is near parabolic around the equilibrium position. The similarity of the three curves indicates that the functionalization of the MOF does not significantly increases the stiffness of the MOF material. As the material is strained beyond 0.05%, the total energy curve becomes non-parabolic. The non-parabolicity and lack of symmetry about the equilibrium position is responsible for the anharmonic phonon response, which can account for high-order dissipation phenomenon beyond the scope of this study.

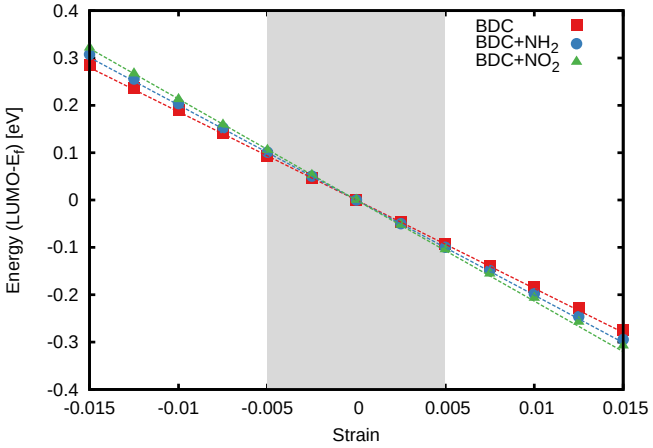

Fig. 3 Plot of the lowest unoccupied orbital (LUMO) as a function of strain. A least square fit of the LUMO as a function of strain was used to estimate the deformation potential (dashed lines). The Fermi level was shifted to zero for all cases. The calculated deformation potential values can be found in Table 1.

3.2 Deformation Potential Calculation

The deformation potential, which will be used in determining the mobility outlined in Equation 1, will be determined in a similar manner to the elastic constant. Actually, the self-consistent results were used to determine the total energy for the elastic constant calculation along with a non-self-consistent field (NSCF) calculation to calculate the density of states (DOS). The DOS calculation was used to determine the location of the conduction band edge and the band-gap. The NSCF calculation were undertaken for all thirteen strain positions between -0.15% and +0.15%. Figure 4 is a visualization of the DOS for all of the thirteen strain positions. The lines in the figure outline the highest occupied molecular orbitals (HOMO), lowest unoccupied molecular orbitals (LUMO), and the Fermi position. It is interesting to note from Figure 4 that as the crystal is compressed, the energy levels converge. Similarly, as the crystal is put in tension, the discrete energy levels diverge. Furthermore, the trend for both the HOMO and LUMO is surprisingly linear. A case was conducted when the crystal was strained in the <100> direction and the linear behavior was not evident.

The 3D deformation potential, E_1, was determined by fitting a linear equation of the LUMO versus strain. The equation takes the following form,

$$E_{LUMO} = E_1 * \varepsilon + E_0, \tag{3}$$

where E_1 is the deformation potential, and ε is the strain. The deformation potential is determined by conducting a least square fit of Equation 3 with E_1 as the independent variable for all three MOF designs. The fit can be visualized in Figure 3. There is a difference between the three functionalizations. The BDC+NO_2 proved to have the largest deformation potential 21.345 eV, followed by BDC+NH_2 and BDC. Recall from Equation 1, the mobility is inversely related to the deformation potential. This finding indicates that the functionalization will decrease the mobility.

3.3 Effective Mass Calculation

The remaining consideration for evaluating Equation 1 is the effective mass. The effective mass consideration is a significant assumption and provides a means of adapting free particle dynamics to an effective medium. Similar to the density of states calculation above for determining the deformation potential, the band structure is determined through a non-self consistent calculation. The only difference is a k-point circuit is defined along the linker path. If a full view of a complete unit cell is taken for the MOF material of interest in this study, the main pathway for electron transport is along the organic linkers to the metalloids. Therefore, it is reasoned that the limiting effective mass will be along these organic linkers and the corresponding k-point path should be defined in this direction. Figure 5 is a plot of the effective mass along the linker from point [110] to [001]. Between all three functionalizations, the effective mass is very similar. It is also determined that the effective mass for the LUMO has two defined minimums associated with the aromatic carbon rings. Fitting the effective mass relation, $E = \hbar k^2/2m^*$, to both of these minimums, the effective mass is determined to be $8.9m_e$. Because the effective mass is greater than unity, the electron will feel more massive resulting in decreased mobility. This can be related through Equation 1 where the effective mass and electron mobility are inversely related. Another interesting finding that comes out of Figure 5 is the flatness of HOMO levels, which confirms the claim by others [13].

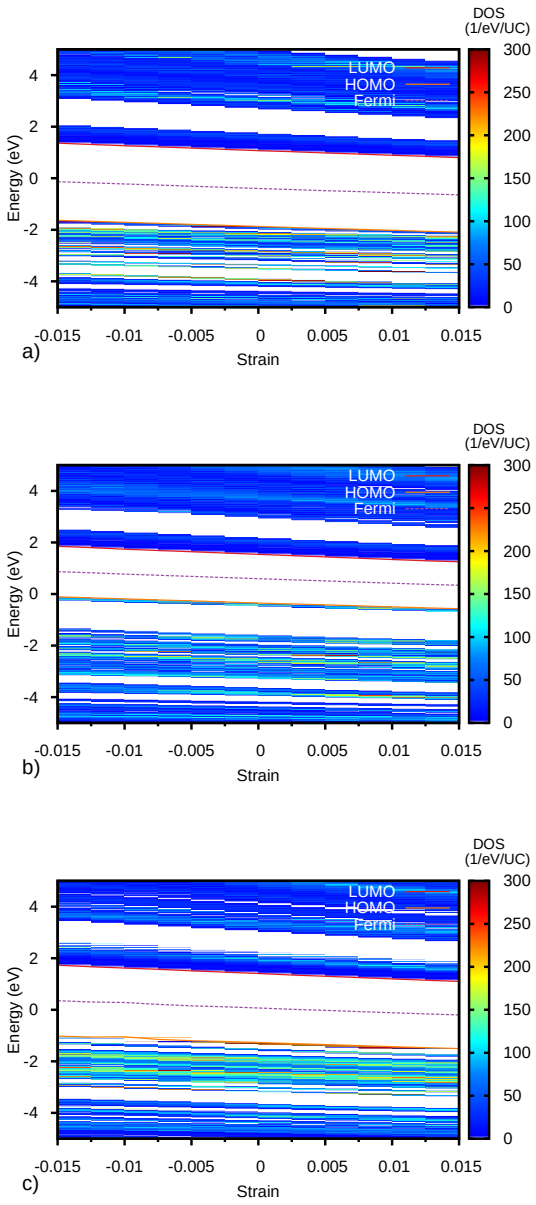

Fig. 4 Density of states plots for the three MOF designs at thirteen strain values ranging from -0.15% to +0.15%. The figures from top to bottom, a) MOF BDC, b) MOF BDC+NH_2, and c) MOF BDC+NO_2. There is a linear slope for both the HOMO and LUMO across the range of strain for all three MOF designs, which was used to calculate a deformation potential (see Figure 3). The band gap for BDC is 3.10eV, BDC+NH_2 is 2.80eV, and BDC+NO_2 is 2.20eV.

3.4 Mobility Calculation

Using the elastic constant, deformation potential, and effective mass, the mobility was calculated using the expression in

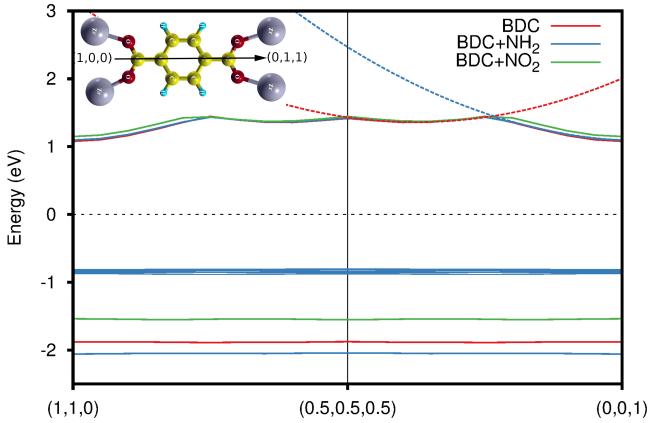

Fig. 5 Plot of the effective mass along the organic linker. The LUMO for all three cases was aligned to demonstrate similarity of curvature between all cases. The effective mass value of 8.9m_e is attributed to the delocalized π electrons of th carbon atoms along the path from [110] to [001]. Note the low curvature of the HOMO states, which corresponds to a low mobility.

Equation 1. The corresponding results are provided in Table 1. The MOF BDC+NO_2 proved to have the lowest mobility of all three designs. The mobility for the BDC+NO_2 case was approximately 1.19x10^{-3} cm^2/V-s. The largest mobility is realized by MOF BDC with a mobility of 1.36x10^{-3} cm^2/V-s. It is evident that the functionalization does influence the mobility, however, the influence in this case is not as significant as the influence on the valance charge population. That being said, what the functionalization provides and is not captured in this study is the increase number of charge carriers.

To provide some confidence to these findings, the mobility values are compared to available literature values. However, pure mobility values are not readily reported in the literature because it requires knowledge of the charge concentration. Furthermore, the exact charge concentration is somewhat nebulous because of the localization of organic structures and temperature dependence of the charge carriers. Often the conductivity is reported and provides some means of comparison for this study. From a experimental point of view, the conductivity can be readily obtained through four point probe measurements of the IV characteristics [13] or more advanced microwave measurements [2,3].

From a computational point of view, the conductivity can be determined from the follow expression, $\sigma = q\mu n$, where σ is the electron contribution to the conductivity, μ is the mobility, which has already been determined, and n is the charge carrier density. The charge density can be estimated from the computed density of states by evaluating the following equa-

tion,

$$n = \int_{LUMO} g(E) f_D(E) dE = \int_{LUMO} \frac{g(E) dE}{1 + exp\left[(E - E_f)/k_B T\right]}, \quad (4)$$

where the charge density is the integral of the density of states, $g(E)$, and the Fermi-Dirac distribution, $f_D(E)$. The density of states $g(E)$ is determined from the results provided in Figure 4. For this calculation, the Fermi level was assumed to be intrinsically in the middle of the band gap. The Fermi location from the DFT calculation is actually shifted towards LUMO, indicating a donor nature of the functionalization and a temperature dependent activation energy, which has been experimentally confirmed[1,4]. In the high temperature limit, the activation will approach $E_g/2$, reassuring our mid-gap Fermi assumption.

The estimate for the charge density at 300K is provided in Table 1 along with the accompanying conductivity predictions. It is noted that the highest concentration is for BDC+NO_2 even though the band gap is smallest for BDC+NH_2. This is an interesting finding as the donor nature of the functionalization influences the LUMO states and in turn the band gap does not dominate the carrier concentration as conventional wisdom may suggest. Using the calculated donor concentration and the mobility, an estimate for the conductivity can be calculated as reported in Table 1. For all of the cases the mobility dominates the conductivity trend resulting in the BDC having the highest mobility and correspondingly the highest conductivity. The next highest conductivity is for BDC+NH_2 followed by BDC+NO_2. Overall, the functionalization in this study corresponds to less than 2% change in conductivity.

In comparison to known literature values such as MOF based tetrathiafulvalene tetrabenzoic acid (H_4TTFTB) with metalloid including Co, Zn, Mn, and Cd[13] the highest conductivity value reported was $2.86\text{x}10^{-4}$ S/cm for Cd_4TTFTB. The lowest conductivity reported value for Zn_2TTFTB was $3.95\text{x}10^{-6}$ S/cm. Similarly, for 2,5- disulfhydrylbenzene-1,4-dicarboxylic acid (H_4DSBDC), the conductivity was reported to range between 10^{-13} and 10^{-6}[1]. These reported values are within the range of the calculated values reported in this study.

Overall, the findings from this study indicate that the functionalization will slightly diminish the mobility as a result of the increase electron-phonon scattering, which was determined through calculated deformation potential. However, a more significant aspect of the functionalization is the ability to tailor the donor concentration near the LUMO. While the band-gap is an important aspect for light absorption, from a electron mobility point of view, the concentration of states near the LUMO, which ultimately contributes to the donor concentration is a more important aspect. Therefore, the objective for tailoring the mobility should focus on the controlling the number of states near the LUMO through functionalization. This argument can be framed from the point of view of the effective mass where the curvature of the lowest band is synonymous with the number of states. While this argument is valid for particle based band motion, these claims will require further investigation when the transport mode is based on electron hopping. That being said, it is hypothesized that in order to design MOF materials with conductivity values on the order of moderately doped semiconductors, the mode of transport must not be electron hopping dominated but rather dominated by electron tunneling along short chains with low effective mass.

4 Conclusion

The approach taken in this study was to use DFT and Boltzmann theory with the relaxation time approximation to compare the mobility for three MOF designs. It was confirmed that the delocalized π electrons in the aromatic ring of the linker provide band-link motion along the path. The mobility trended to decrease with functionalization the charge concentration increased with functionalization. The overall prediction for the conductivity decreased as a result of the decreased mobility, which was 14% larger for BDC+NO_2 compared to BDC. The most significant of the findings was that the functionalization actually increases the number of states near the LUMO. This resulted in increased charge density and highlighted the most advantageous avenue for increasing the conductivity in MOF based materials. It was concluded that in order to design MOF based materials with conductivity values on the order of moderately doped semiconductors the transport must be tunneling based along short chains with functionalizaton that contributes to high carrier concentrations. Future consideration beyond particle based theory is required to account for quantum mechanical and higher order interactions, which is required to analyze the large scope of metal-organic structures.

References

1 L. Sun, C. H. Hendon, M. A. Minier, A. Walsh and M. Dinca, *Journal of the American Chemical Society*, 2015, **137**, 6164–6167.

2 T. Narayan, T. Miyakai, S. Seki and M. Dinca, *Journal of the American Chemical Society*, 2012, **134**, 12932–12935.

3 A. Saeki, Y. Koizumi, T. Aida and S. Seki, *Accounts of chemical research*, 2012, **45**, 1193–1202.

4 A. A. Talin, A. Centrone, A. C. Ford, M. E. Foster, V. Stavila, P. Haney, R. A. Kinney, V. Szalai, F. El Gabaly, H. P. Yoon *et al.*, *Science*, 2014, **343**, 66–69.

5 V. Stavila, A. A. Talin and M. D. Allendorf, *Chem. Soc. Rev.*, 2014, **43**, 5994–6010.

6 L. Valenzano, B. Civalleri, S. Chavan, S. Bordiga, M. H. Nilsen, S. Jakobsen, K. P. Lillerud and C. Lamberti, *Chemistry of Materials*, 2011, **23**, 1700–1718.

7 S. Bordiga, C. Lamberti, G. Ricchiardi, L. Regli, F. Bonino, A. Damin, K.-P. Lillerud, M. Bjorgen and A. Zecchina, *Chemical communications*, 2004, 2300–2301.

8 H.-C. Zhou, J. R. Long and O. M. Yaghi, *Chemical reviews*, 2012, **112**, 673–674.

9 L.-M. Yang, P. Vajeeston, P. Ravindran, H. Fjellvag and M. Tilset, *Inorganic chemistry*, 2010, **49**, 10283–10290.

10 Y. Kobayashi, B. Jacobs, M. D. Allendorf and J. R. Long, *Chemistry of Materials*, 2010, **22**, 4120–4122.

11 M.-H. Zeng, Q.-X. Wang, Y.-X. Tan, S. Hu, H.-X. Zhao, L.-S. Long and M. Kurmoo, *Journal of the American Chemical Society*, 2010, **132**, 2561–2563.

12 N. J. Tao, *Nat Nano*, 2006, **1**, 173–181.

13 S. S. Park, E. R. Hontz, L. Sun, C. H. Hendon, A. Walsh, T. Van Voorhis and M. Dinca, *Journal of the American Chemical Society*, 2015, **137**, 1774–1777.

14 H. Wu, Y. S. Chua, V. Krungleviciute, M. Tyagi, P. Chen, T. Yildirim and W. Zhou, *Journal of the American Chemical Society*, 2013, **135**, 10525–10532.

15 J. Long, S. Wang, Z. Ding, S. Wang, Y. Zhou, L. Huang and X. Wang, *Chem. Commun.*, 2012, **48**, 11656–11658.

16 Y. Hu, S. Xiang, W. Zhang, Z. Zhang, L. Wang, J. Bai and B. Chen, *Chem. Commun.*, 2009, 7551–7553.

17 G. Zhang and C. B. Musgrave, *The Journal of Physical Chemistry A*, 2007, **111**, 1554–1561.

18 T. Musho, J. Li and N. Wu, *Phys. Chem. Chem. Phys.*, 2014, **16**, 23646–23653.

19 S. Grimme, *Journal of Computational Chemistry*, 2006, **27**, 1787–1799.

20 V. Barone, M. Casarin, D. Forrer, M. Pavone, M. Sambi and A. Vittadini, *Journal of Computational Chemistry*, 2009, **30**, 934–939.

21 J. Bardeen and W. Shockley, *Phys. Rev.*, 1950, **80**, 72–80.

22 S. Devautour-Vinot, G. Maurin, C. Serre, P. Horcajada, D. Paula da Cunha, V. Guillerm, E. de Souza Costa, F. Taulelle and C. Martineau, *Chemistry of Materials*, 2012, **24**, 2168–2177.

23 R. Warmbier, A. Quandt and G. Seifert, *The Journal of Physical Chemistry C*, 2014, **118**, 11799–11805.